



# Highly stable UiO-66-NH<sub>2</sub> by the microwave-assisted synthesis for solar photocatalytic water treatment

Rafael R. Solís<sup>a,b,\*</sup>, Manuel Peñas-Garzón<sup>a</sup>, Carolina Belver<sup>a</sup>, Juan J. Rodríguez<sup>a</sup>, Jorge Bedia<sup>a</sup>

<sup>a</sup> Department of Chemical Engineering, Universidad Autónoma de Madrid, Cantoblanco, 28049 Madrid, Spain

<sup>b</sup> Department of Chemical Engineering, Universidad de Granada, Granada 18071, Spain

## ARTICLE INFO

Editor: Dr. G. Palmisano

### Keywords:

UiO-66-NH<sub>2</sub>  
Linker leaching  
Microwave synthesis  
Pharmaceuticals  
Photocatalysis

## ABSTRACT

This work introduces the novel use of a highly stable UiO-66-NH<sub>2</sub> in water with a linker release less than 0.2‰ (per-mile) in a wide pH range. The MOF was prepared by a fast microwave-assisted method comparing for the first time the effect of two Zr precursors: Zr oxychloride and organic Zr alkoxide; with synthesis temperatures 120–180 °C. The use of oxychloride as Zr precursor led to a MOF with bigger particle and crystal size than the Zr alkoxide. The sample prepared with ZrOCl<sub>2</sub> at 140 °C resulted in the best crystallinity, highest textural definition (area 875 m<sup>2</sup> g<sup>-1</sup>, pore volume 0.39 cm<sup>3</sup> g<sup>-1</sup>), good optical properties for solar radiation absorption (bandgap 2.88 eV), and the highest photoactivity to remove sulfamethoxazole in water. The activity of the optimum UiO-66-NH<sub>2</sub> sample was assessed in a continuous flow experiment, testing the ability of the simultaneous degradation of a six pharmaceutical mixture fed at a more realistic environmental scenario (500 µg L<sup>-1</sup> each). The MOF showed an outstanding stability over 20 h with no detectable release of linker and high removal efficiency.

## 1. Introduction

The study and development of Metal Organic Frameworks (MOFs) has experienced great growth for the last two decades. MOFs are iso-reticular metal-organic structures composed of a metal cluster and organic linker that can be flexibly tuned providing materials with extremely high developed surface area, controlled porosity, versatile adsorption capacity, and great optical properties as semiconductor, among others [1]. Diverse applications have been proposed for the application of these materials beyond their initial purposes, such as gas adsorption and storage [2], biomass transformation [3], sensors [4], drug delivery [5], heterogeneous catalysis [6,7], and semiconductors for photocatalytic applications such as energy production [8] or water treatment [9].

The use of MOFs has recently launched interest in the field of water purification since these materials display excellent adsorption ability [10] and promising photocatalytic behavior [11] in the removal of anthropogenic organic pollutants, such as the contaminants of emerging concern. These contaminants are well known to be persistent in the environment and their removal in the released points, mainly wastewater treatment plants [12], is not well addressed yet [13]. An adequate treatment of these contaminants is mandatory to face the challenges of

water resources and to responsibly reintroduce the reused resources into a circular economy [14]. Accordingly, the development of new strategies to efficiently clean water, such as the environmental catalysis based in MOFs, may lead to new routes and solutions to the water pollution problem. Among the vast list of MOFs developed to date, UiO-66 (named after the University of Oslo) is a Zr-MOF with high photocatalytic activity [15] and a decade of career. More importantly over other MOFs, UiO-66 is a high water-stable MOF [16,17], the main problem to face when using these materials for water-based applications [18,19]. Recently, the amino functionalized UiO-66, namely UiO-66-NH<sub>2</sub>, has proved to enhance the optical properties harvesting the absorption of radiation to the visible region [20].

This work reports the synthesis and photocatalytic assessment of UiO-66-NH<sub>2</sub>. This MOF is usually prepared using inorganic salts of Zr, although some recent works are exploring the possibility of the use of organic precursors [21]. Due to the lack of information, this work aims to compare the use of Zr oxychloride and Zr alkoxide in terms of MOF formation and the photocatalytic activity. The materials have been prepared by assisted-microwave heating, which considerably shortens the synthesis time of the conventional solvothermal method from hours to minutes. To our knowledge, there are no previous studies that compare the effect of the nature of the Zr precursor in the preparation of

\* Corresponding author at: Department of Chemical Engineering, Universidad Autónoma de Madrid, Cantoblanco, 28049 Madrid, Spain.

E-mail addresses: [rafael.rodriguez@uam.es](mailto:rafael.rodriguez@uam.es), [rafarsolis@ugr.es](mailto:rafarsolis@ugr.es) (R.R. Solís).

UiO-66-NH<sub>2</sub>, with no available studies about the possibility of an organic Zr source such as an alkoxide. Almost all the works use inorganic salts of Zr for the preparation [15]. Two different variables have been studied in the synthesis process, the nature of the Zr source and the temperature in the microwave synthesis. In the first case, two different sources were considered; an organic Zr alkoxide, i.e. Zr(OC<sub>4</sub>H<sub>9</sub>)<sub>4</sub>, and Zr oxychloride (ZrOCl<sub>2</sub>·8 H<sub>2</sub>O). Regarding the temperature, in both precursors, a range within 120–180 °C was explored. A complete set of characterization techniques (XRD, N<sub>2</sub> isotherm, STEM, TEM, XPS, DRS-UV-vis, and pH<sub>pzc</sub>) was performed. The resulting MOFs have been tested as photocatalysts for sulfamethoxazole degradation under simulated solar irradiation. The effects of the synthesis variables on the properties of the resulting MOFs and their catalytic behavior were studied. The stability of this sample in water solution at various pH values (2–11) was analyzed in terms of the linker released (2-amino-terephthalic acid). A plausible mechanism of photo-activation was tentatively proposed based on a complete scavenger study and analysis for the location of the electronic bands of the solid. Finally, as a novel aspect to assess the photocatalytic performance and lack of deactivation, a continuous flow test was applied with the best UiO-66-NH<sub>2</sub> sample for the removal of a mixture of six pharmaceuticals in a continuous long-term experiment (20 h on stream), which thus far is a very scarcely used approach in photocatalytic tests.

## 2. Experimental section

### 2.1. Chemicals and synthesis of UiO-66-NH<sub>2</sub> by microwave-assisted method

All chemicals used were acquired from Sigma-Aldrich® and used without further purification. HPLC grade acetonitrile was used as a mobile phase. Solutions were prepared with ultrapure water with a resistivity of 18.2 MΩ cm.

The UiO-66-NH<sub>2</sub> samples were synthesized by solvothermal method assisted by microwave irradiation. The synthesis procedure was adapted from the literature [22–27] and two different sources of zirconium were evaluated as precursors in the study, i.e. zirconium oxychloride (ZrOCl<sub>2</sub>·8 H<sub>2</sub>O) and zirconium butoxide (Zr(OC<sub>4</sub>H<sub>9</sub>)<sub>4</sub>). Briefly, 1.5 mmol of 2-aminoterephthalic acid (ATA) and 43 mL of *N,N*-dimethylformamide (DMF) were added to a Teflon lined vessel of 75 mL, keeping under vigorous magnetic stirring. Next, 1.5 mmol of zirconium source, i.e. ZrOCl<sub>2</sub>·8 H<sub>2</sub>O or Zr(OC<sub>4</sub>H<sub>9</sub>)<sub>4</sub>, were incorporated into the solution. Finally, 7 mL of acetic acid completed the final volume. In the case of ZrOCl<sub>2</sub>·8 H<sub>2</sub>O, 286 μL of HCl (37%) were added. After 15 min of stirring, the vessels were hermetically closed and heated with microwave radiation in a multimode FlexiWave station (Milestone®). The vessels were heated under autogenous pressure with microwave radiation until reaching the desired temperature (120–180 °C) in 7 min and kept thereafter during a holding time of 30 min and finally cooled down to room temperature. As a result, a pale yellowish solid was generated and collected by centrifugation (5 min, 4000 rpm). Two washing steps with DMF, consisting of magnetic stirring for 20 min, were carried out. The washed solid was dried under vacuum atmosphere overnight (16 h, 80 °C). For complete elimination of occluded DMF and unreacted ATA, the dried samples were thermally treated (200 °C, 16 h, air atmosphere) as previously suggested during the preparation of this [28] and other MOFs such as NH<sub>2</sub>-MIL-125(Ti) [19].

### 2.2. Characterization of the materials

The confirmation of the crystalline structure was carried out by X-Ray Diffraction (XRD) in a Bruker® D8 advance device with Lynxeye XE-T detector, equipped with a Cu Kα source. The angle 2θ was monitored within 2–50 ° with a scan step of 1.8 ° min<sup>−1</sup>. The crystal structure was corroborated using the Crystal Open Database and the software Match!®, whereas the XRD pattern of the standard was simulated with Vesta®.

The textural properties were analyzed by N<sub>2</sub> adsorption-desorption performed at −196 °C in a Tristar 123 equipment (Micromeritics® II 3020). The specific surface area was estimated by the BET method (S<sub>BET</sub>), whereas the t-plot method was used to assess the external or non-microporous surface area and the volume of micropores (S<sub>EXT</sub> and V<sub>MP</sub>, respectively). The microporous surface was calculated by difference between the S<sub>BET</sub> and the S<sub>EXT</sub>. The pore size distribution was obtained by the density functional theory (DFT).

The morphology of the UiO-66-NH<sub>2</sub> nanoparticles was assessed by Field Emission Scanning Electron Microscopy (FE-SEM) in a Hitachi S-4800 device equipped with a Scanning Transmission Electron detector (STEM). Moreover, a Transmission Electron Microscopy (TEM) technique was used for the same purpose in Tecnai T20 equipment. Before the analysis, the samples were suspended in methanol and deposited in a copper (STEM) or carbon (TEM) grid.

The optical properties were studied in a UV-visible Diffuse Reflectance Spectroscopy (UV-vis DRS) using a Shimadzu UV2600 spectrophotometer. The bandgap of the resulting semiconductors was estimated by Tauc's plot method and indirect transitions [29], estimating the Kubelka–Munk function (F(R<sub>∞</sub>)) and depicting (F(R<sub>∞</sub>)·hν)<sup>1/2</sup> vs the energy of the absorbed photons [30,31]. The photoluminescence (PL) technique was used to assess the recombination effect. The PL emission spectra were measured in a Varian Cary Eclipse fluorescence spectrophotometer (Agilent®), with 370 nm as the excitation wavelength and the emission spectra recorded within 400–550 nm.

The electrochemical properties of the UiO-66-NH<sub>2</sub> samples were measured by using Metrohm Autolab potentiostat (PGSTAT204). The electrodes were the Metrohm DropSens ITO10, using an indium tin oxide (ITO), carbon and silver as working, counter and reference electrodes, respectively, and the measure was carried out inside a Metrohm Faraday cage. The suspensions of the samples (1 mg mL<sup>−1</sup>) were prepared in 0.5 M Na<sub>2</sub>SO<sub>4</sub> as the supporting electrolyte (pH ~5.4 at 25 °C) and placed into the electrochemical cell. The effectiveness of the electron-hole charge separation was assessed by the Nyquist plot of the electrochemical impedance spectroscopy (EIS) data. The flat band potential was estimated by the Mott-Schottky plot under applied potential within −1.5 and 0.4 V and scan frequency of 10 and 100 Hz. The flat band potential (V<sub>FB</sub>) was calculated from the intersection of the tangent in the ascendant line with the abscissa axis (V) in the representation of 1/C<sup>2</sup> (C, the space charge capacitance) vs the potential [32]:

$$V_{FB(NHE,pH)} = V_0 - \frac{k \cdot T}{e}, \quad (1)$$

where V<sub>FB (NHE,pH)</sub> is the flat band potential at the pH medium, V<sub>0</sub> is the potential at 1/C<sup>2</sup> = 0, k the Boltzmann's Constant, and T the operation temperature. The obtained V<sub>FB</sub> was corrected to normal hydrogen electrode (NHE) reference by adding the redox potential of Ag/AgCl (ΔV<sub>Ag/AgCl</sub> = 0.21 V). Finally, a Nernstian shift (0.059 V/pH unit) of the resulting value was applied to correct the measure to pH = 7 [33]. Then, the potential of the conduction band referred to NHE at pH = 7 (V<sub>CB</sub>) was calculated as follows [34]:

$$V_{CB} \approx V_{FB(NHE,pH=7)} = V_{FB(NHE,pH)} + \Delta V_{Ag/AgCl} - 0.059 (7 - pH) \quad (2)$$

The semi-quantitative surface analysis was carried out by X-ray Photoelectron Spectroscopy (XPS) in a PHI VersaProbe II device, emitting an X-ray source from Al Kα source. The software XPSpeak 4.1® was used for the deconvolution of the peaks, considering a Shirley background and correction of C1s to adventitious carbon at 284.6 eV.

The pH value at the point of zero charge (pH<sub>pzc</sub>) was calculated by a drift method [35]. Briefly, solutions of 50 mL containing NaCl 0.1 M were prepared and the pH adjusted to the desired value within 2 and 10 (pH<sub>initial</sub>) by adding NaOH or HCl of 0.1, 1 or 10 M, depending on the initial pH value to reach. Next, 150 mg of the UiO-66-NH<sub>2</sub> sample was added (3 g L<sup>−1</sup>) and kept under stirring until for 24 h, measuring the pH thereafter (pH<sub>final</sub>). The pH<sub>pzc</sub> was calculated as the intersection of the

curve of  $\text{pH}_{\text{final}}$  versus  $\text{pH}_{\text{initial}}$  with the bisector.

### 2.3. Photocatalytic degradation tests

The photocatalytic activity of the prepared UiO-66-NH<sub>2</sub> samples was assessed as the ability of the degradation of sulfamethoxazole (SMX) in water. A solar simulator Suntest XLS+ (ATLAS®) equipped with a Xe lamp and emitting at 600 W m<sup>-2</sup> radiation over 320 nm (indoor ID65 filter) was used in the photodegradation tests. A jacketed glass reactor kept at 25 °C was placed inside the simulator, containing 250 mL of water solution with the required dose of the photocatalyst (250 mg L<sup>-1</sup>). In the batch tests, the adsorption equilibrium between the target compound and the photocatalyst was reached before switch on the light by maintaining the solid under stirring for 30 min. After that, the reactor was irradiated with the solar simulated radiation, and aqueous samples were extracted at regular periods. The photocatalyst was removed by filtration (PVDF filters, 0.45 µm). Experiments were carried out by triplicate and the average value was taken. The relative standard deviation was lower than 5%. For the continuous flow experiments, an inlet feeding was coupled to the setup by pumping the initial solution (mixture of six pharmaceuticals) at a rate of ca. 1 mL min<sup>-1</sup>. A paper filter was coupled to the outlet to avoid the loss of the MOF during the reaction. A scheme of the experimental continuous flow setup can be seen in the Fig. S1. The effect of pH on the photocatalytic activity of UiO-66-NH<sub>2</sub> was tested by adjusting the pH to 3, 5 and 9 with NaOH or HCl 0.1 M. The effects of common inorganic anions was checked at representative concentrations of these species (2.50 mM of Cl<sup>-</sup>, 0.83 mM of NO<sub>3</sub><sup>-</sup> or 3.07 mM of HCO<sub>3</sub><sup>-</sup>) after biological treatment [36].

The concentration of sulfamethoxazole in the aqueous solution, initially 5 mg·L<sup>-1</sup>, was quantified by HPLC equipped with a Diode Array detector (SPD-M30A) in a Shimadzu Prominence LC-2030C chromatograph. The stationary phase consisted of a C18 Eclipse Plus column (5 µm, Agilent). The mobile phase, pumped at a rate of 0.7 mL min<sup>-1</sup>, was a mixture of 57% acetonitrile and 43% acidified water (0.1% v/v acetic acid). A volume of 30 µL was injected and the quantification was performed at a wavelength of 260 nm. The release of the linker, e.g. ATA, was monitored by using the same chromatographic method and wavelength, but increasing the injection volume to 90 µL. The limit of detection (LOD) [37] determined for SMX and ATA were, respectively according to the above methods, 138 and 68 µg L<sup>-1</sup>. For the simultaneous separation and quantification of the mixture of six pharmaceuticals, initially 500 µg L<sup>-1</sup> each, a gradient program was used. Thus, a flow rate of 0.8 mL min<sup>-1</sup> was fed with a composition of acetonitrile (A) and acidified water (0.1% v/v acetic acid, B) from initially 5–95% of A in 30 min, and kept at 95% for 5 min. The following absorption wavelengths were used for the quantification, i.e. 243 nm acetaminophen (ACE), 275 nm ciprofloxacin (CIP), 276 nm tetracycline (TCL), 260 nm sulfamethoxazole (SMX), 276 nm diclofenac (DCF), and 220 nm ibuprofen (IBU). The LOD values estimated for this multi-component method were 9, 55, 32, 18, 23, and 54 µg L<sup>-1</sup> for ACE, CIP, TCL, SMX, DCF, and IBU, respectively.

ESR spin-trap experiments were performed in a Bruker EMX (X band) spectrometer with the ER4123D dielectric resonator using a capillary quartz tube. The UV irradiation in situ ESR measurements was carried out with a high-pressure mercury lamp (Bruker, UV Irradiation System, ER 203 UV). The instrumental settings were as follows: center field = 3480 G; sweep width = 300 G; microwave power = 0.2 mW; modulation amplitude = 10 G; modulation frequency = 100 kHz; receiver gain = 1.261·10<sup>4</sup>; time constant = 81.92 ms; sweep time = 20.97 s; resolution in x = 1024 points; number of scans = 1. 2,2,6,6-tetramethyl-1-piperidinyloxy (TEMPO) was used to carry out the in situ ESR spin-trap experiments. The capillary tube was filled with 10 µL of a water/TEMPO solution (2 mM) containing the catalyst suspended in a ratio 0.250 µg/µL. The capillary tube was irradiated inside the cavity for 15 min, recording spectra every 5 min. Similar experiments were carried out with 5,5-dimethyl-1-pyrroline N-oxide (DMPO), using a

solution water/DMPO (2 mM) or methanol/DMPO (2 mM) for the detection of HO· and O<sub>2</sub>· radicals, respectively.

## 3. Results and discussion

### 3.1. Effect of nature of the Zr precursor and the synthesis temperature

The MOF UiO-66-NH<sub>2</sub> was prepared by solvothermal method controlling the nucleation and growing of crystallites by heating through microwave radiation. This methodology considerably reduces the synthesis time required in the conventional solvothermal method. Different variables may influence the crystallinity of the resulting material such as temperature, holding time, and nature of the metal precursor, i.e. Zr oxychloride or Zr butoxide. Although the holding time affects the definition of the structure of the MOF, a preliminary study (results not shown) revealed that holding time during the synthesis within 30 min and 1 h did not display a difference in the definition of the structure, keeping constant the rest of the variables. Accordingly, this study was focused on the interpretation of the effect of the temperature (120–180 °C) and the nature of zirconium sources, i.e. ZrOCl<sub>2</sub> and Zr(OC<sub>4</sub>H<sub>9</sub>)<sub>4</sub>, on the crystallinity definition of the material. The XRD diffractograms of the resulting UiO-66-NH<sub>2</sub> samples are depicted in Fig. 1. The standard pattern of UiO-66-NH<sub>2</sub> (COD- 4348132 [38]) was selected to study the accurate crystallization of the MOF, characterized by two intense peaks; one located at 2θ = 7.38–7.40° corresponding to the plane (111) and a second peak of lower intensity at 2θ = 8.3° assigned to the (200) plane [38]. All synthesized samples fit well this pattern. The greater intensity of the peaks reveals a better crystallization of the MOF structure if ZrOCl<sub>2</sub> is used in the synthesis. The use of the zirconium alkoxide conducts to XRD peaks of lower intensity, characteristic of a poorer crystallization degree. This aspect was also quantified with the estimation of the crystal size by the Scherrer's equation, see Table 1. A ~2.7 folded crystal size was registered for the MOF prepared with ZrOCl<sub>2</sub> (10 ± 2 nm) in comparison with the prepared with Zr alkoxide (3.7 ± 0.4 nm). The synthesis temperature did not significantly affect the crystal size.

The N<sub>2</sub> adsorption-desorption isotherms at -196 °C were obtained to analyze the textural properties of the prepared UiO-66-NH<sub>2</sub> samples. The isotherms (Fig. 2 A and B) revealed a sharp N<sub>2</sub> uptake at low relative pressures characteristic of a type I isotherm, typical of a microporous material. Table 1 shows the specific surface areas, i.e. BET and microporous calculated from the t-plot method, and the total and micropore volumes. The UiO-66-NH<sub>2</sub> samples prepared with ZrOCl<sub>2</sub> led to samples with higher developed microporosity than those made with Zr(OC<sub>4</sub>H<sub>9</sub>)<sub>4</sub>. The synthesis temperature did not exert a crucial effect in the definition of the porosity with the Zr(OC<sub>4</sub>H<sub>9</sub>)<sub>4</sub> precursor although a slight higher surface area was observed in the sample synthesized at 160 °C. However, in the case of the use of ZrOCl<sub>2</sub>, the temperature shows more influence on porous structure, reaching a maximum of surface area and micropore volume at 160 and 140 °C, respectively. In general trend, when using ZrOCl<sub>2</sub>, a bimodal pore size distribution with average values around 1.0 and 1.5–2.0 nm was observed (Fig. 2A<sub>1</sub>). In contrast, when the organic precursor is used, mostly all the samples displayed unimodal pore distribution with most of the pores in the range of 1.0–1.3 nm. The MOF UiO-66-NH<sub>2</sub> prepared with ZrOCl<sub>2</sub> as precursor consists of a microporous material that can reach specific surface areas typically up to 900 m<sup>2</sup> g<sup>-1</sup> [39,40] although some exceptionally higher values have been reported in the literature (~1100 m<sup>2</sup> g<sup>-1</sup> [24]).

The optical properties of the prepared UiO-66-NH<sub>2</sub> samples were studied by UV-vis DRS absorption. Fig. 3 compares the UV-vis spectra as a function of the synthesis variables used, i.e. zirconium precursor and synthesis temperature. All solids show similar spectra, with the characteristic absorption peaks of the UiO-66-NH<sub>2</sub>. The UV-vis profile of this MOF exhibits a band located at 200–260 and a well-defined peak at ~365 nm [41]. The band can be attributed to the ligand-to-metal charge transfer, origin of the photo-activation mechanism from the O atoms of

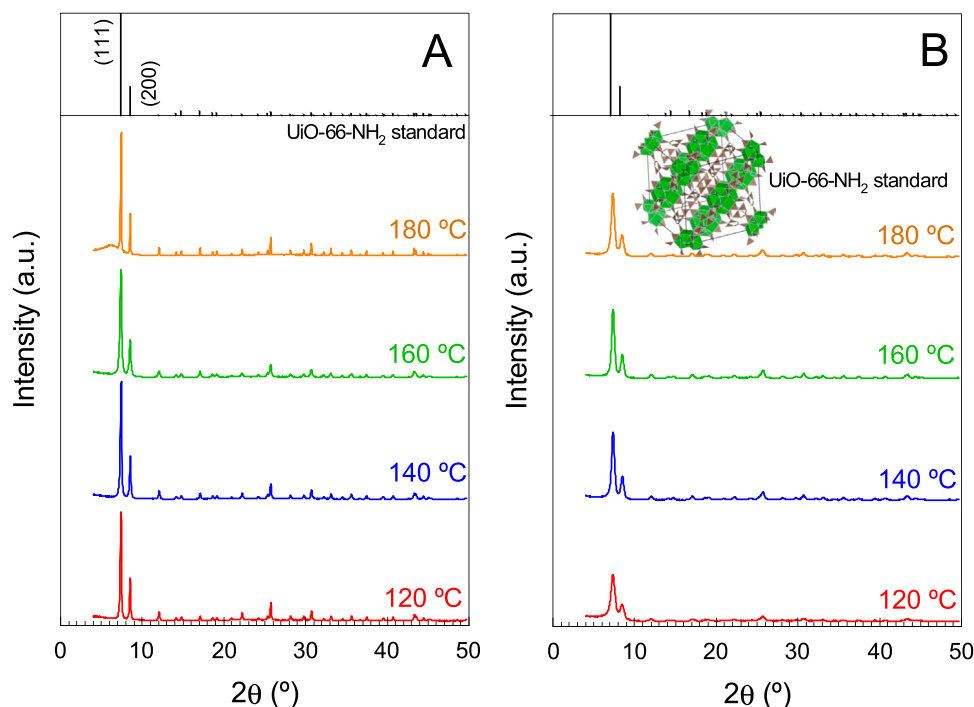


**Fig. 1.** XRD patterns of UiO-66-NH<sub>2</sub> prepared at different temperatures (120–180 °C) for ZrOCl<sub>2</sub> (A) and Zr alkoxide (B) as zirconium precursors. UiO-66-NH<sub>2</sub> standard form ref. [38] (COD-4348132) and the corresponding unit cell depicted with Vesta®.

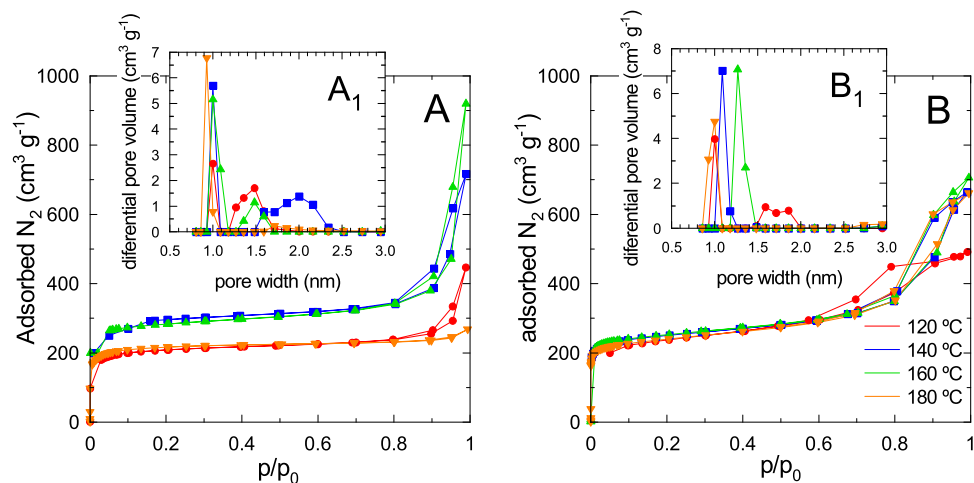


**Fig. 2.** N<sub>2</sub> adsorption-desorption isotherms at – 196 °C of UiO-66-NH<sub>2</sub> prepared with ZrOCl<sub>2</sub> (A) and Zr(OC<sub>4</sub>H<sub>9</sub>)<sub>4</sub> (B), and their corresponding pore size distribution (A<sub>1</sub> and B<sub>1</sub>).

**Table 1**

Characterization properties of the prepared UiO-66-NH<sub>2</sub> samples.

Precursor	Temperature (°C)	Crystal size <sup>1</sup> (nm)	S <sub>BET</sub> (m <sup>2</sup> ·g <sup>-1</sup> )	S <sub>MIP</sub> (m <sup>2</sup> ·g <sup>-1</sup> )	V <sub>total</sub> <sup>2</sup> (cm <sup>3</sup> ·g <sup>-1</sup> )	V <sub>MIP</sub> (cm <sup>3</sup> ·g <sup>-1</sup> )	Bandgap (eV)
ZrOCl <sub>2</sub>	120	9.6	583	520	0.69	0.25	2.75
	140	9.6	875	710	1.11	0.39	2.88
	160	7.1	935	722	1.42	0.35	2.90
	180	14.4	712	577	0.41	0.28	2.90
Zr(OC <sub>4</sub> H <sub>9</sub> ) <sub>4</sub>	120	3.2	770	443	0.76	0.22	2.84
	140	4.1	825	463	1.03	0.27	2.84
	160	4.1	831	575	1.09	0.28	2.86
	180	3.6	793	517	1.02	0.25	2.85

<sup>1</sup>Estimated from the peak of the (111) plane by the Scherrer equation.

<sup>2</sup>Calculated from the maximum N<sub>2</sub> uptake at p/p<sub>0</sub>~0.99



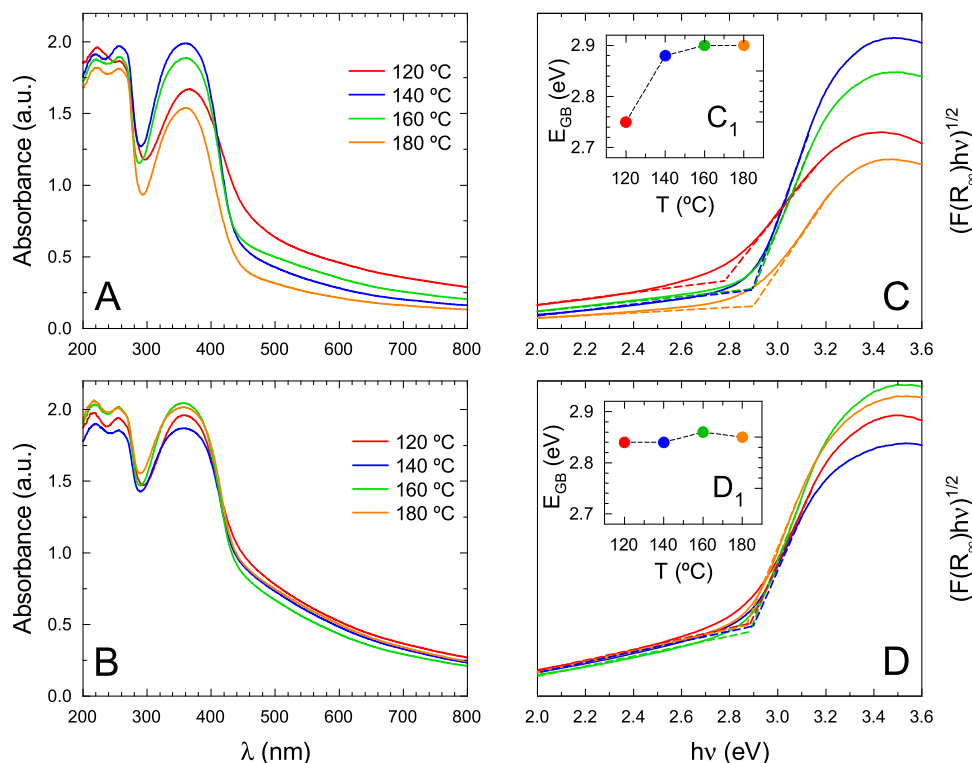


**Fig. 3.** UV-visible DRS absorption spectra of UiO-66-NH<sub>2</sub> samples prepared with ZrOCl<sub>2</sub> (A) and Zr(OC<sub>4</sub>H<sub>9</sub>)<sub>4</sub> (B) and their corresponding Tauc's plot for the calculation of the bandgap energy (subfigures C-D, respectively) and evolution of the bandgap value with the synthesis temperature (subfigures C<sub>1</sub> and D<sub>1</sub>, respectively).

the organic linker (ATA) to the Z oxo-cluster [42,43]. The peak centered at 365 nm is due to the interaction of the lone pair of electrons of amino group with the  $\pi^*$ -orbital of benzene ring [44]. If the nature of the precursor is compared, the organic Zr source led to UV-vis spectra with more absorption in the visible range, whereas those prepared with ZrOCl<sub>2</sub> generated spectra with a more pronounced decay over 420–440 nm, especially at higher synthesis temperatures. The bandgap energy was estimated from these spectra following the Tauc's plot method for indirect transitions. According to the Tauc's plot

(Fig. 3C-C<sub>1</sub>), an increase of the bandgap energy is observed if the temperature is raised, see values in Table 1, reaching a maximum value at 2.90 eV. On the other hand, the samples prepared with Zr(OC<sub>4</sub>H<sub>9</sub>)<sub>4</sub> displayed less sensitivity with the synthesis temperature, being the bandgap values between 2.84 and 2.86 eV. It can be summarized that the nature of the precursor does not affect significantly to the bandgap value, only the crystallinity is modified, as discussed before.

The morphology of the prepared nanoparticles was assessed by STEM and TEM microscopies in those samples prepared at 140 °C, since this

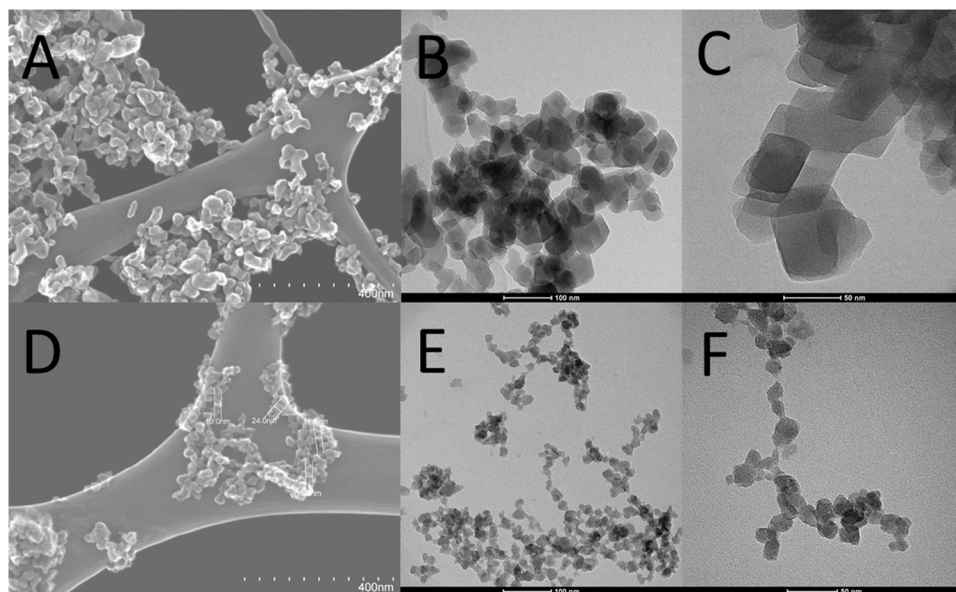


**Fig. 4.** STEM (A and D) and TEM (B, C, E, F) micrographs of UiO-66-NH<sub>2</sub> samples prepared at 140 °C with ZrOCl<sub>2</sub> (top subfigures, A-C) and Zr(OC<sub>4</sub>H<sub>9</sub>)<sub>4</sub> (bottom subfigures, D-F).

temperature seems to be optimal for the highest crystallization and best textural properties. The Zr precursor affects the particle size as can be seen in Fig. 4. In the case of the MOF prepared with the Zr oxychloride, the particles present sizes within 20–50 nm, whereas in the case of organic Zr this range drops to 15–20 nm. Similar particle sizes have been reported in the literature for this MOF prepared under microwave irradiation [45]. The microwave synthesis promotes the formation of hot spots as a consequence of the direct heating of the solvent, in contrast to the heat transmission by conduction in the wall of a vessel reactor with the conventional procedure. As a result, the process is much faster and leads to smaller particle size if compared to the traditional [46]. In contrast, the conventional heating synthesis leads to larger particles also due to the larger synthesis times [22]. If the two precursors are compared, it can be deduced from the lower particle size that the organic  $\text{Zr}(\text{OC}_4\text{H}_9)_4$  precursor promotes the nucleation rate in comparison to the growing rate. The UiO-66- $\text{NH}_2$  nanoparticles are characterized by an octahedral shape [24,47], in this work these nanoparticles are smoothed in the edges and appear aggregated in bigger groups. Moreover, as observed in Fig. 4, the fact of small nanoparticles linked to building bigger aggregates suggests fast nucleation if compared to the growth rate during the microwave heating process [48].

The surface chemical composition of UiO-66- $\text{NH}_2$  prepared with  $\text{ZrOCl}_2$  (at 140 °C) was evaluated by XPS. The obtained XPS surveys (see Fig. 5) confirm the expected composition of UiO-66- $\text{NH}_2$  with some details regarding the oxygen and nitrogen groups. According to the formula of UiO-66- $\text{NH}_2$ , i.e.  $\text{Zr}_{24}\text{O}_{120}\text{H}_{192}\text{H}_9\text{N}_{24}$ , the atomic ratio Zr:O should be 0.20 and experimentally was quantified as  $\sim 0.18$ . Likewise, the Zr:N ratio, was 1.4 instead of 1.0. The high-resolution spectra of the element regions provided detailed information, especially regarding the O and N groups. The C 1s peak was successfully fitted to four contributions corresponding to C-C (284.6 eV), C-N (285.0 eV), C=C (285.7 eV), and  $\text{COO}^-$  (288.8 eV) [49,50]. The presence  $\text{Zr}^{4+}$

oxidation state was corroborated in Zr 3d spectra with two shifted peaks attributed to  $3d_{3/2}$  (184.9 eV) and  $3d_{5/2}$  (182.6 eV) [47]. The N 1s peak was deconvoluted into two, commonly identified as an amino group ( $-\text{NH}_2$ , 399.1 eV) and the protonated amidogen ( $-\text{NH}_3^+$ , 399.9 eV) [45, 47]. In the spectrum of O 1s [51], an important contribution C=O bonds (532.0 eV) was observed if compared the Zr-O bonds (530.9 eV).

### 3.2. Photocatalytic degradation tests

#### 3.2.1. Effect of synthesis temperature and nature of Zr precursor on SMX degradation

The photocatalytic activity of the prepared UiO-66- $\text{NH}_2$  samples was studied in the degradation of the antibiotic SMX, whose presence is frequently reported in wastewater effluents [12]. A set of preliminary tests to assess the plausible adsorption of SMX onto the MOF was done (results not shown), due to the potential high ability of these materials to adsorb aqueous pollutants [10,52,53]. Nevertheless, in this case, the removal of SMX by adsorption was low. Accordingly, before the photocatalytic degradation, an adsorption step was carried out to establish the adsorption equilibrium onto the surface of the solid. Fig. 6 depicts the temporal evolution of the normalized concentration of SMX for the prepared photocatalysts in the presence of solar radiation. As it can be observed, the adsorption elimination was minimal, ca. 10% under the conditions tested. A blank test of photolysis ( $\lambda > 320$  nm) was accomplished to corroborate the lack of degradation by the sole action of solar radiation. The photocatalytic process led to the abatement of the antibiotic, 90% of initially  $5 \text{ mg L}^{-1}$  in the best case.

In the samples prepared with  $\text{ZrOCl}_2$ , an important effect of the synthesis temperature is observed, with an optimum pseudo-first order rate constant at 140 °C ( $k = 0.29 \pm 0.02 \text{ h}^{-1}$ ). The better textural properties, i.e. microporosity, of this sample if compared to the rest, may explain the outstanding photocatalytic activity of this sample. Based on

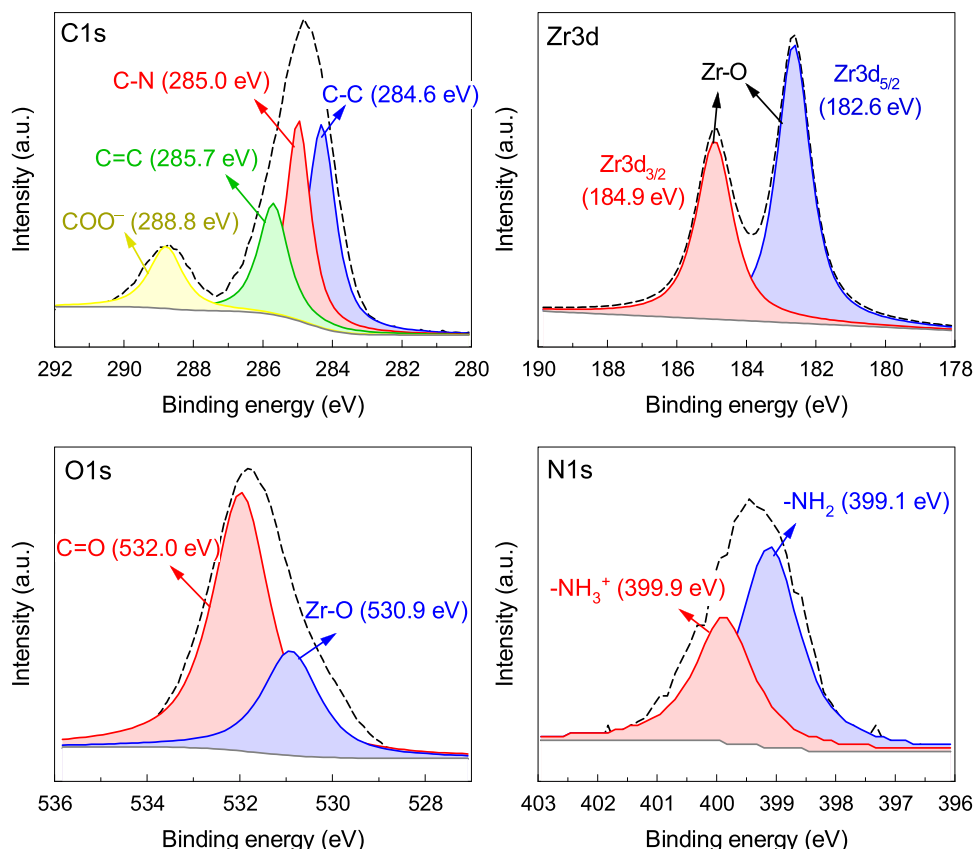
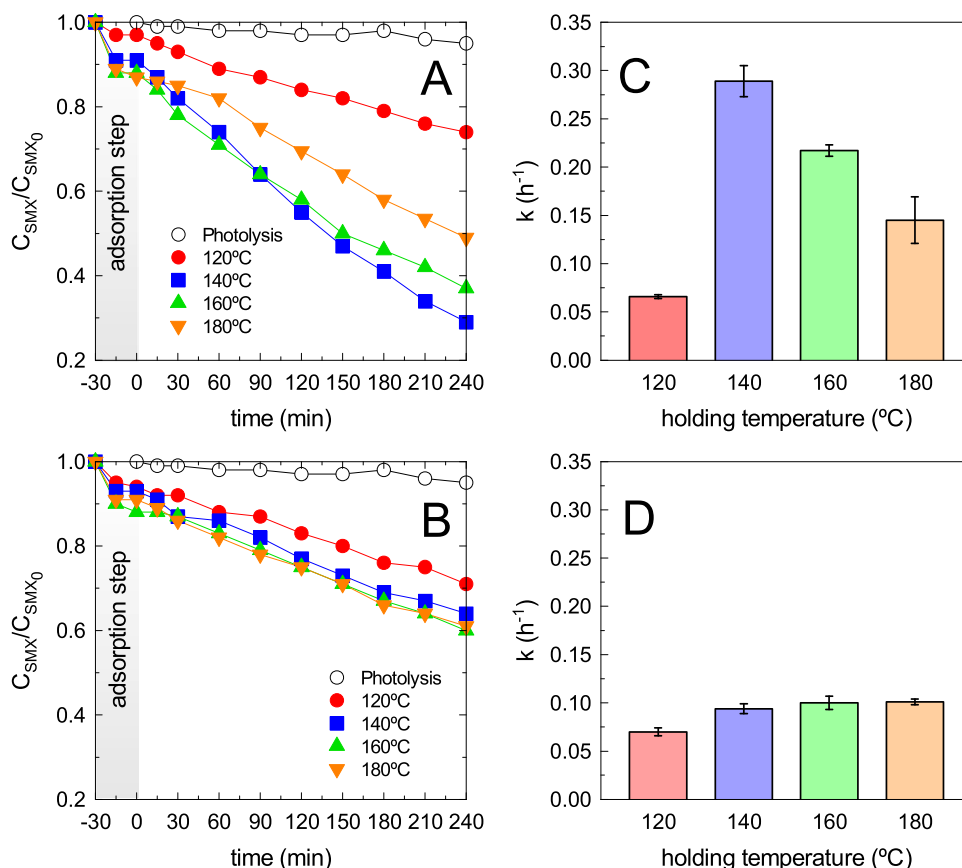


Fig. 5. Surface chemical characterization by XPS of the UiO-66- $\text{NH}_2$  sample prepared with  $\text{ZrOCl}_2$  at 140 °C.



**Fig. 6.** Time-course of the normalized concentration of SMX during the photocatalytic degradation with UiO-66-NH<sub>2</sub> prepared at different synthesis temperatures with  $ZrOCl_2$  (A) and  $Zr(OC_4H_9)_4$  (B), and their corresponding pseudo-first order rate constants (C and D). Experimental conditions:  $V = 250$  mL;  $C_{SMX,0} = 5$  mg L<sup>-1</sup>,  $C_{UiO-66-NH_2} = 250$  mg L<sup>-1</sup>;  $T = 25$  °C,  $pH = 5.6 \pm 0.2$ .

this fact, the UiO-66-NH<sub>2</sub> sample prepared with  $ZrOCl_2$  at 140 °C was selected for further analyses. Great differences were registered if the Zr precursors used in the MOF synthesis are compared. The UiO-66-NH<sub>2</sub> samples synthesized with the Zr alkoxide displayed much lower activity than those prepared with  $ZrOCl_2$ . The evolution of the concentration was successfully fitted to pseudo-first order kinetics ( $R^2 > 0.99$ ). The use of  $ZrOCl_2$  led to a semiconductor with higher activity, the pseudo-first order rate constant ( $k$ ) was almost 3 folded if compared to the organic Zr source. The value of  $k$  was in the range of the reported in the literature for UiO-66-NH<sub>2</sub> with other pharmaceuticals, see Table S1, within 0.02–0.60 h<sup>-1</sup> depending on the target compound.

The improved photo-activity can be attributed to the higher crystallinity reached when using  $ZrOCl_2$  in the synthesis, since the optical properties, i.e. bandgap, are very similar for the both precursors. The PL technique was applied to compare the recombination effect in the samples prepared at 140 °C with both Zr precursors. The PL spectrum, see Fig. S2, depicts a lower intensity peak for the UiO-66-NH<sub>2</sub> prepared with oxychloride which means a lower recombination effect and contributes to explain the higher photoactivity observed in SMX degradation. To further explain the different photocatalytic activity observed, the electrochemical impedance spectroscopy (EIS) was applied to analyze the charge transfer resistance on the surface of the MOF. In general, the arc radius of the Nyquist plots of EIS represents the reaction rate over the working electrode [54]. As depicted in the Fig. 7, the UiO-66-NH<sub>2</sub> sample prepared with  $ZrOCl_2$  presented smaller radius of the semicircle of EIS than the made with  $Zr(OC_4H_9)_4$ , revealing accelerated separation of charges and lower interfacial electron transfer resistance. This enhanced behavior of the sample prepared with  $ZrOCl_2$  contributes to explain the better photocatalytic activity during SMX degradation.

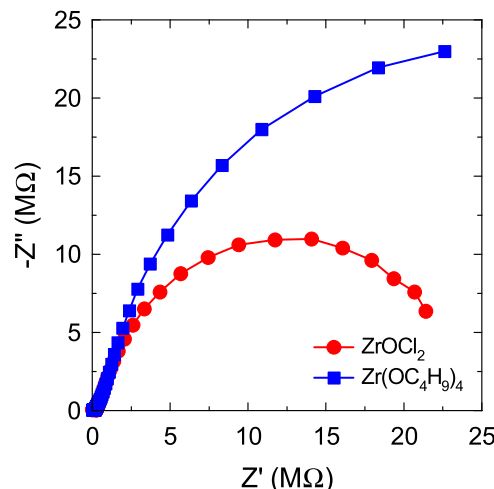


**Fig. 7.** Influence of Zr precursor in the EIS Nyquist plots for UiO-66-NH<sub>2</sub> at 140 °C.

### 3.2.2. Effects of pH and inorganic anions in the photocatalytic activity of SMX

The effect of pH was studied given the relevance of this variable in the photocatalytic performance, triggered by the adsorption of the target compound on the catalyst's surface. The UiO-66-NH<sub>2</sub> sample prepared with  $ZrOCl_2$  at 140 °C was tested at pH values of 3, 5 and 9. The results are depicted in Fig. S3. The differences can be explained from the electrostatic interaction between SMX and the surface of the MOF. The

SMX molecule shows two speciation equilibria, with  $pK_1 = 1.74$  between the cationic and neutral forms and a  $pK_2 = 5.7$  between the neutral and the anionic species. A value of the  $pH_{pzc} = 4.28$  (see Fig. S4) was estimated for the MOF by the drift method, i.e. the surface of the catalyst is negatively charged over this pH value. At  $pH = 3$ , according to the speciation diagram of SMX,  $\sim 5\%$  is positively charged as  $SMX^+$  and the surface of the MOF is also positively charged. This potential electric repulsion can explain the decrease of the kinetic rate constant respect the value to  $pH = 5$ , closer to the neutral conditions for both the SMX molecule and MOF surface. At  $pH = 9$ , both the pharmaceutical and the MOF surface are negatively charged, causing their repulsion and resulting in a lower kinetic constant.

The presence of inorganic anions usually results detrimental on the photocatalytic performance. Several tests were carried out in the presence of common inorganic anions, such as chloride, nitrate and carbonate at common environmental concentrations [36]. The results (see Fig. S3) show the impact of these inorganic anions on SMX degradation. Thus, the observed rate constants decreased in the order blank > chloride > nitrate > bicarbonate with very low difference among them. Similar behavior has been reported previously for the degradation of SMX with other photocatalysts, such as  $TiO_2$  [55]. These anions can be adsorbed on the active sites of the MOF and react with the species photo-generated on the catalyst surface, i.e.  $h^+$ ,  $HO^\bullet$  or  $O_2^{\bullet-}$ , competing with SMX for them [56]. The decrease reactive species leads to a less effective oxidation in presence of those anions.

### 3.2.3. Elucidation of the oxidative route of SMX

The mechanism of the photocatalytic oxidation of SMX was tentatively screened by the use of potential scavengers that inhibit the

plausible routes of the process. The results are depicted in Fig. 8A. Firstly, the contribution of  $HO^\bullet$  was analyzed with the addition of *tert*-butyl alcohol (TBA) since it reacts with  $HO^\bullet$  with a rate constant of  $6.8 \cdot 10^9 \text{ M}^{-1} \text{ s}^{-1}$  [57]. Despite 10 mM of TBA was added, a very slight decrease in the degradation profile of SMX was monitored; hence, the pseudo-first order rate constant of SMX removal was almost unchanged, i.e.  $0.29 \pm 0.02 \text{ h}^{-1}$  of the test blank vs  $0.24 \pm 0.03 \text{ h}^{-1}$  in the TBA presence. The role of the superoxide radical, generated during the reduction of the absorbed  $O_2$  by the photo-generated electrons was studied by adding tiron (sodium 1,2-dihydroxybenzene, 3-5-disulfonate) [58], a  $O_2^{\bullet-}$  scavenger (rate constant with  $O_2^{\bullet-}$ ,  $5 \cdot 10^8 \text{ M}^{-1} \text{ s}^{-1}$  [59]) that also reacts with  $HO^\bullet$  ( $10^9 \text{ M}^{-1} \text{ s}^{-1}$  [60]). However, since the test with TBA shows that the role of  $HO^\bullet$  is marginal, the use of tiron allows to establish the  $O_2^{\bullet-}$  contribution. Fig. 8A shows that the addition of tiron did not affect the SMX degradation profile and the temporal evolution of SMX was overlapped the corresponding TBA curve. Consequently, the role of superoxide radical seems to be negligible in the SMX degradation. Oxalic acid was considered as a hole scavenger. Oxalate has been postulated as a good hole scavenger due to the low reactivity towards  $HO^\bullet$  ( $1.5 \cdot 10^7 \text{ M}^{-1} \text{ s}^{-1}$  [61]) or to the photo-generated electrons ( $3.5 \cdot 10^7 \text{ M}^{-1} \text{ s}^{-1}$  [61]) if compared to other similar hole scavengers such as iodide or *iso*-propyl alcohol [58]. In the presence of 10 mM oxalic acid, the pseudo-first order rate constant of SMX decreased to  $0.14 \pm 0.01 \text{ h}^{-1}$ . Since the role of  $HO^\bullet$  can be discharged, the importance of  $h^+$  as the main oxidative species of SMX must be highlighted. Finally, a test in the presence of  $AgNO_3$  was completed as photo-generated electrons inhibitor. The addition of  $Ag^+$  showed a considerable enhancement to the blank test. This behavior can be ascribed to the ability of  $Ag^+$  to catch electrons, minimizing therefore the undesirable recombination effect of

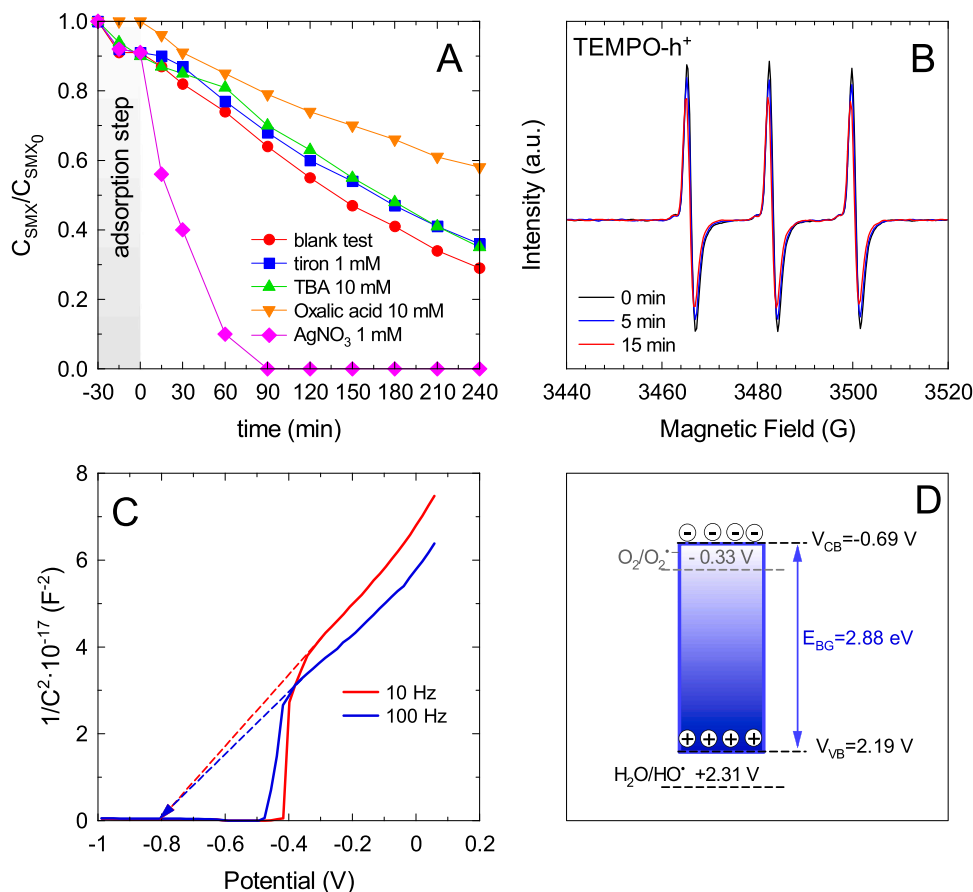


**Fig. 8.** A) Time-course of the normalized concentration of SMX during the photocatalytic degradation with the optimum UiO-66-NH<sub>2</sub> sample (ZrOCl<sub>2</sub>, 140 °C) in the presence of scavengers. Experimental conditions:  $V = 250 \text{ mL}$ ;  $C_{SMX,0} = 5 \text{ mg L}^{-1}$ ,  $C_{UiO-66-NH_2} = 250 \text{ mg L}^{-1}$ ;  $T = 25^\circ \text{C}$ ,  $pH_0 = 5.5 \pm 0.4$ . B) ESR analysis of TEMPO- $h^+$ . C) Mott-Schottky plot for the determination of the flat band potential. D) Bands alignment proposal for UiO-66-NH<sub>2</sub>.



the photo-generated electron-hole pair and reducing  $\text{Ag}^+$  onto the surface [62]. ESR spin-trap experiment employing TEMPO was used for characterizing the holes generated during the UiO-66- $\text{NH}_2$  photoexcitation. TEMPO is a spin molecule with a stable triplet ESR spectrum that can be reduced by holes, resulting in a decrease in the ESR signal strength [63,64]. The decrease of TEMPO- $\text{h}^+$  ESR intensity upon irradiation is evident in this system (Fig. 8B), confirming that the photo-degradation is controlled by holes. ESR in situ experiments were also performed with DMPO to detect the presence of  $\text{HO}^\bullet$  and  $\text{O}_2^\bullet$  radicals [65]. In both cases, no ESR signals were observed after 15 min of irradiation.

To propose a schematic diagram of the photocatalytic process, the bands alignment was established according to the position of the conduction band by electrochemical characterization. The flat band potential of the sample UiO-66- $\text{NH}_2$  ( $\text{ZrOCl}_2$ , 140 °C) was determined from the Mott-Schottky as  $-0.80$  V (Fig. 8C). After normalization to NHE scale at  $\text{pH}=7$ , the conduction band potential ( $V_{\text{CB}}$ ) was  $-0.69$  V. The bandgap energy of this sample was determined as  $E_{\text{BG}}=2.88$  eV. The potential of the valence band ( $V_{\text{VB}}$ ) was determined taking the bandgap energy into account:

$$V_{\text{VB}} = V_{\text{CB}} + \frac{E_{\text{BG}}}{e}, \quad (3)$$

whereas 'e' is the charge of the electron. The proposal of bands location is schematized in Fig. 8D. The  $V_{\text{CB}}$  is more negative than the redox potential of the pair  $\text{O}_2/\text{O}_2^\bullet$  ( $-0.33$  V vs NHE at  $\text{pH}=7$  [66]). Although the formation of the superoxide is energetically possible according to the band alignment, the use of tiron as scavenger discharged its influence. The formation of hydroxyl radical is not expected since the holes generates display a lower potential value than the required for the water molecule oxidation ( $\text{H}_2\text{O}/\text{HO}^\bullet$ ,  $+2.31$  V vs NHE at  $\text{pH}=7$  [67]). The photo-generated holes would be, therefore, the responsible species for the SMX degradation.

### 3.2.4. Stability of UiO-66- $\text{NH}_2$ in water at different pH values

There are very few works that analyze the stability of MOFs in water in terms of metal or linker leaching. Buzek et al. [16] have recently analyzed the linker and  $\text{Zr}^{4+}$  release of UiO-66 in aqueous media in the presence of different buffers [68]. Their results suggest the MOF is stable in water, e.g. the linker release and  $\text{Zr}^{4+}$  is below the LOD of their analysis in water; however, under extreme conditions of buffer concentration UiO-66 slightly starts to collapse. Apart from this work, in the specific case of UiO-66-based materials, the main information available in the literature is mostly regarding the changes of the structure after water contact [68–71]. The lack of loss of crystallinity by XRD or textural properties (BET area) indicate the high stability of this MOF in water, even after a long period such as 12 months [68,71]. Nevertheless, these techniques are not conclusive as they do not provide quantitative results in terms of species released into the aqueous solution.

To provide detailed information about the linker leaching, in this work the stability of the UiO-66- $\text{NH}_2$  ( $\text{ZrOCl}_2$ , 140 °C) was assessed by keeping it in an aqueous solution under vigorous stirring for a long period, i.e. 24 h. The study was carried out at different pH values and the concentration of the linker, i.e. ATA, was quantified after that period. To quantify the release of the organic linker, the ATA leaching was expressed as the percentage of the ATA released from the ATA contained in the structure of the MOF. The formula of the unitary cell is described as  $\text{Zr}_{24}\text{O}_{120}\text{C}_{192}\text{H}_{96}\text{N}_{24}$  [72], in which 24 molecules of ATA ( $\text{C}_8\text{H}_7\text{O}_4\text{N}$ ) are contained. Accordingly, the ATA leached can be calculated as:

$$\text{ATA leached (\%)} = \frac{C_{\text{ATA}}}{C_{\text{UiO66-NH}_2}} \frac{M_{\text{UiO66-NH}_2}}{24 \times M_{\text{ATA}}} \times 100, \quad (4)$$

where  $M_{\text{UiO-66-NH}_2}$  ( $6848 \text{ g mol}^{-1}$ ) and  $M_{\text{ATA}}$  ( $181 \text{ g mol}^{-1}$ ) are the molar masses of UiO-66- $\text{NH}_2$  and ATA, respectively; and  $C_{\text{UiO-66-NH}_2}$  and  $C_{\text{ATA}}$  their respective concentration in the aqueous solution.

From the results of Fig. 9, it can be deduced a high stability of this MOF in an aqueous solution. All ATA values were below  $1 \text{ mg L}^{-1}$ , with an important decrease at  $\text{pH} > 3$ . It was necessary to increase the MOF dose in the aqueous solution, i.e.  $3 \text{ g L}^{-1}$ , to release ATA up to the limit of detection of the analysis ( $68 \mu\text{g L}^{-1}$ ). The release was approximately 3 times higher at  $\text{pH}=2$  if compared to the rest of pH range studied (3–11). If results are normalized in terms of ATA content in the structure of the dosed solid MOF, less than 0.2 per-mille (‰) was observed at  $\text{pH} > 3$ . This data confirms the high stability of UiO-66- $\text{NH}_2$  in water in a wide range of pH values as similarly reported for UiO-66 [16].

### 3.2.5. Photocatalytic activity and stability of UiO-66- $\text{NH}_2$ in continuous flow test

The activity and stability of the photocatalytic performance of the sample UiO-66- $\text{NH}_2$  prepared with  $\text{ZrOCl}_2$  at a synthesis temperature of 140 °C were further assessed for the removal of a mixture of six pharmaceuticals, i.e. ACE, CIP, TCL, SMX, DCF and IBU. The use of MOFs under continuous flow operation would be desirable from a practical point of view. Whereas much efforts have been devoted to the application of MOFs in catalytic heterogeneous reactions in liquid phase [73], there are very few works dealing with continuous flow photocatalysis [29,74]. In the current work continuous flow mode was used for the photocatalytic treatment of a mixture of compounds at low concentrations, e.g. close to their environmental occurrence. Fig. 10A depicts the temporal evolution of the conversion reached in each case. Three of them were completely removed in the first 30 min, i.e. CIP, TCL, IBU. The rest were removed following the order  $\text{DCF} > \text{SMX} > \text{ACE}$ . The MOF displayed great stability after the steady-state was reached with no loss of the photocatalytic activity as the monotonical evolution demonstrates. Furthermore, the lack of leached ATA at the outlet of the photoreactor, i.e. no detectable peak in the HPLC analysis was observed, enforces the possibility of the use for a long time. The structural stability of the solid was tested by analyzing the XRD patterns of the fresh and used samples. The Fig. S5 shows that the 20 h-used catalyst maintains high crystallinity and complete definition of the whole diffraction pattern of UiO-66- $\text{NH}_2$ . Moreover, the textural properties of this used catalyst were characterized by  $-196$  °C  $\text{N}_2$  adsorption-desorption (see Fig. S6). The BET area remained almost unchanged ( $875$  initially vs  $884 \text{ m}^2 \text{ g}^{-1}$  after 20 h of use). The same for the micropore volume ( $0.39\text{--}0.35 \text{ cm}^3 \text{ g}^{-1}$ ), with a pore size distribution very similar to the fresh sample. These results corroborate the high stability of the catalyst after the 20 h experiment.

The great differences in the performance of the pharmaceutical conversion can be attributed to the electrostatic interactions required to the adsorption of the target compounds, required for triggering the photocatalytic reactions. The assessment of the possible surface

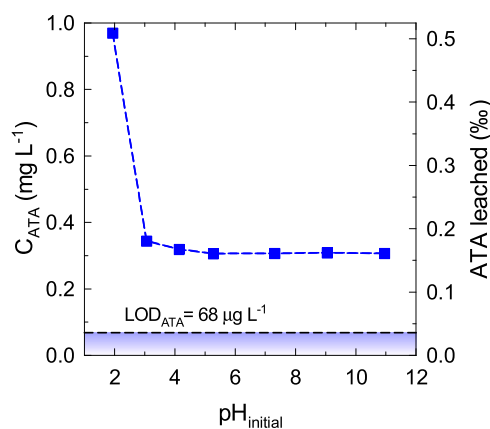
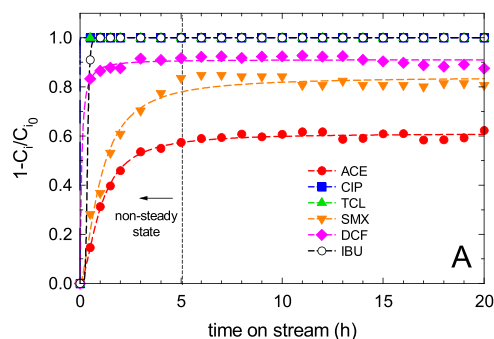


Fig. 9. Release ATA after 24 h of contact in water at different pH values with the optimum UiO-66- $\text{NH}_2$  sample ( $\text{ZrOCl}_2$ , 140 °C). Experimental conditions:  $V=50 \text{ mL}$ ,  $C_{\text{UiO-66-NH}_2}=3.0 \text{ g L}^{-1}$ .



**Fig. 10.** Conversion of the pharmaceuticals tested upon time on stream in a continuous flow experiment with the optimum UiO-66-NH<sub>2</sub> (ZrOCl<sub>2</sub>, 140 °C). Experimental Conditions:  $V = 250$  mL;  $Q = 1.0$  mL·min<sup>-1</sup>;  $C_{i,0} = 500$  µg·L<sup>-1</sup> (each),  $C_{\text{UiO-66-NH}_2} = 250$  mg·L<sup>-1</sup>;  $T = 25$  °C,  $\text{pH}_0 \sim 5.0$ .

electrostatic interactions can be useful to make an initial screening, although other contributions could participate during the adsorption step such as hydrogen bonds [75],  $\pi$ - $\pi$  interactions [53]; or additional degradation by photolysis at  $> 320$  nm, as in the specific case of tetracycline [76] or ciprofloxacin [77], verified in batch experiments (results not shown). A value of the  $\text{pH}_{\text{pzc}} = 4.28$  was estimated for the UiO-66-NH<sub>2</sub> (ZrOCl<sub>2</sub>, 140 °C) MOF by the drift method, e. g. the surface of the catalyst is negatively charged over this pH value. According to the speciation of the tested pharmaceuticals [75], at  $\text{pH} = 5$  CIP is positively charged (CIP<sup>+</sup>, 98%) and TCL is under in the same situation but to less extent (TCL<sup>+</sup>, 6%). On the other side, SMX and DCF are partially dissociated with contributions of the negatively charged species, i.e. 17% and 88%, respectively. This fact explains why CIP and TCL are completely removed whereas DCF and SMX are just partially eliminated. In the case of ACE, whose acid-base species are neutral under the experimental conditions, the lack of electrostatic attraction may explain the lesser photocatalytic degradation depicted in Fig. 10. The results observed for IBU cannot be explained by the sole consideration of electrostatic interactions. IBU performs a high photocatalytic removal, comparable to CIP and TCL, under the action of UiO-66-NH<sub>2</sub>. At the working pH value (5), IBU is negatively charged (33% of IBU<sup>-</sup>). However, it has been reported that this molecule can undergo adsorption via hydrogen bonding into the -NH<sub>2</sub> of the MOF [75] and, that therefore, would explain the high affinity to launch the reaction.

#### 4. Conclusions

The UiO-66-NH<sub>2</sub> can be easily prepared by microwave-assisted synthesis. From the two Zr precursors used, ZrOCl<sub>2</sub> was more convenient due to the better crystallinity obtained if compared to the Zr alkoxide. The synthesis temperature seems not to be a crucial variable in the synthesis process, being temperatures over 140 °C enough to define the high crystallinity, well-developed porosity, and optical properties. The sample prepared with ZrOCl<sub>2</sub> at 140 °C performed the highest photocatalytic activity during the removal of sulfamethoxazole (pseudo-first order constant,  $0.29$  h<sup>-1</sup>), probably due to the better definition of the crystal and textural properties. The Zr alkoxide led to a MOF with crystal sizes  $\sim 2.7$  times smaller and particles sizes also considerable smaller ZrOCl<sub>2</sub>. Moreover, this material presented outstanding high stability in aqueous solution in a wide range of pH values, with the leaching of the linker below  $0.2$  per-mille (‰), which confers great competitiveness towards other MOFs, usually unstable in water. The photocatalytic mechanism was tentatively elucidated by a detailed scavenger study during sulfamethoxazole degradation, suggesting a clear role played by the photo-generated holes. Finally, the UiO-66-NH<sub>2</sub> was tested in a continuous flow experiment with a mixture of six pharmaceuticals frequently reported as contaminants of emerging concern. This novel approach provides information on the feasibility of using this

MOF in long-term experiments in a continuous setup. The optimized sample of UiO-66-NH<sub>2</sub> performed a stable photocatalytic activity beyond 20 h of time on stream. No detectable presence of the organic ligand in the aqueous solution was registered and the conversion reached after the steady-state was kept constant. From the six pharmaceuticals tested, ciprofloxacin, tetracycline and ibuprofen were easily removed and diclofenac  $>$  sulfamethoxazole  $>$  acetaminophen displayed a decreasing conversion. These results demonstrate the possibility of the application of this metal-organic framework in water treatment over long periods of treatment.

#### CRediT authorship contribution statement

**Rafael R. Solís:** Conceptualization, Methodology, Investigation, Writing – original draft. **Manuel Peñas-Garzón:** Conceptualization, Methodology, Investigation, Writing – review & editing. **Carolina Belver:** Conceptualization, Investigation, Writing – review & editing, Supervision, Funding acquisition. **Juan J. Rodríguez:** Writing – review & editing, Supervision, Funding acquisition. **Jorge Bedia:** Conceptualization, Writing – review & editing, Supervision. All authors have read and agreed to the published version of the manuscript.

#### Declaration of Competing Interest

The authors declare that they have no known competing financial interests or personal relationships that could have appeared to influence the work reported in this paper.

#### Acknowledgments

Rafael Rodríguez Solís is grateful to the Spanish Ministry of Science, Innovation and Universities for his postdoctoral contract (*Juan de la Cierva Formación*, Ref. FJC2018-035513-I). Manuel Peñas Garzón acknowledges the Spanish Ministry of Education, Culture and Sports for his predoctoral contract (Ref. FPU16/00576) contracts. This research was funded by the Spanish State Research Agency (PID2019-106186RB-I00/AEI/10.13039/501100011033, Spain). The authors are also grateful to the supporting analyses provided by the external services of the Autonomous University of Madrid (SIdI), University of Extremadura (SAIUEx), University of Zaragoza (SAI), University of Málaga (SCAI) and Universidad Complutense of Madrid (CAI).

#### Appendix A. Supporting information

Supplementary data associated with this article can be found in the online version at doi:10.1016/j.jece.2021.107122.

#### References

- [1] J. Gascon, A. Corma, F. Kapteijn, F.X. Llabrés, I. Xamena, Metal organic framework catalysis: quo vadis? ACS Catal. 4 (2014) 361–378, <https://doi.org/10.1021/cs400959k>.
- [2] A.R. Millward, O.M. Yaghi, Metal-organic frameworks with exceptionally high capacity for storage of carbon dioxide at room temperature, J. Am. Chem. Soc. 127 (2005) 17998–17999, <https://doi.org/10.1021/ja0570032>.
- [3] R. Fang, A. Dhakshinamoorthy, Y. Li, H. Garcia, Metal organic frameworks for biomass conversion, Chem. Soc. Rev. 49 (2020) 3638–3687, <https://doi.org/10.1039/D0CS00070A>.
- [4] H.Y. Li, S.N. Zhao, S.Q. Zang, J. Li, Functional metal-organic frameworks as effective sensors of gases and volatile compounds, Chem. Soc. Rev. 49 (2020) 6364–6401, <https://doi.org/10.1039/c9cs00778d>.
- [5] S. Rojas, P. Horcajada, Understanding the incorporation and release of salicylic acid in metal-organic frameworks for topical administration, Eur. J. Inorg. Chem. 2021 (2021) 1325–1331, <https://doi.org/10.1002/ejic.202001134>.
- [6] A. Bavykina, N. Kolobov, I.S. Khan, J.A. Bau, A. Ramirez, J. Gascon, Metal-organic frameworks in heterogeneous catalysis: recent progress, new trends, and future perspectives, Chem. Rev. 120 (2020) 8468–8535, <https://doi.org/10.1021/acs.chemrev.9b00685>.
- [7] A. Dhakshinamoorthy, Z. Li, H. Garcia, Catalysis and photocatalysis by metal organic frameworks, Chem. Soc. Rev. 47 (2018) 8134–8172, <https://doi.org/10.1039/C8CS00256H>.

- [8] A. Dhakshinamoorthy, A.M. Asiri, H. García, Metal-organic framework (MOF) compounds: photocatalysts for redox reactions and solar fuel production, *Angew. Chem. Int. Ed.* 55 (2016) 5414–5445, <https://doi.org/10.1002/ANIE.201505581>.
- [9] J. Bedia, V. Muelas-Ramos, M. Peñas-Garzón, A. Gómez-Avilés, J.J. Rodríguez, C. Belver, A review on the synthesis and characterization of metal organic frameworks for photocatalytic water purification, *Catalysts* 9 (2019) 52, <https://doi.org/10.3390/catal9010052>.
- [10] Y. Pi, X. Li, Q. Xia, J. Wu, Y. Li, J. Xiao, Z. Li, Adsorptive and photocatalytic removal of persistent organic pollutants (POPs) in water by metal-organic frameworks (MOFs), *Chem. Eng. J.* 337 (2018) 351–371, <https://doi.org/10.1016/j.cej.2017.12.092>.
- [11] V.K. Sharma, M. Feng, Water depollution using metal-organic frameworks-catalyzed advanced oxidation processes: a review, *J. Hazard. Mater.* 372 (2019) 3–16, <https://doi.org/10.1016/j.jhazmat.2017.09.043>.
- [12] I. Michael, L. Rizzo, C.S. McArdell, C.M. Manaia, C. Merlin, T. Schwartz, C. Dagot, D. Fatta-Kassinos, Urban wastewater treatment plants as hotspots for the release of antibiotics in the environment: a review, *Water Res.* 47 (2013) 957–995, <https://doi.org/10.1016/j.watres.2012.11.027>.
- [13] K. Kümmerer, D.D. Dionysiou, O. Olsson, D. Fatta-Kassinos, A path to clean water, *Science* 361 (2018) 222–224, <https://doi.org/10.1126/science.aau2405>.
- [14] S. Guerra-Rodríguez, P. Oulego, E. Rodríguez, D.N. Singh, J. Rodríguez-Chueca, Towards the implementation of circular economy in the wastewater sector: challenges and opportunities, *Water* 12 (2020) 1431, <https://doi.org/10.3390/w12051431>.
- [15] J. Winarta, B. Shan, S.M. McIntyre, L. Ye, C. Wang, J. Liu, B. Mu, A decade of UiO-66 research: a historic review of dynamic structure, synthesis mechanisms, and characterization techniques of an archetypal metal-organic framework, *Cryst. Growth Des.* 20 (2020) 1347–1362, <https://doi.org/10.1021/acs.cgd.9b00955>.
- [16] D. Bůžek, S. Adamec, K. Lang, J. Demel, Metal-organic frameworks vs. buffers: case study of UiO-66 stability, *Inorg. Chem. Front.* 8 (2021) 720–734, <https://doi.org/10.1039/d0qi00973c>.
- [17] A. Dhakshinamoorthy, A. Santiago-Portillo, A.M. Asiri, H. Garcia, Engineering UiO-66 metal organic framework for heterogeneous catalysis, *ChemCatChem* 11 (2019) 899–923, <https://doi.org/10.1002/CCTC.201801452>.
- [18] A.M. Chávez, A. Rey, J. López, P.M. Álvarez, F.J. Beltrán, Critical aspects of the stability and catalytic activity of MIL-100(Fe) in different advanced oxidation processes, *Sep. Purif. Technol.* 255 (2021), 117660, <https://doi.org/10.1016/j.seppur.2020.117660>.
- [19] A. Gómez-Avilés, V. Muelas-Ramos, J. Bedia, J.J. Rodríguez, C. Belver, Thermal post-treatments to enhance the water stability of NH<sub>2</sub>-MIL-125(Ti), *Catalysts* 10 (2020) 603, <https://doi.org/10.3390/CATAL10060603>.
- [20] L. Shen, R. Liang, M. Luo, F. Jing, L. Wu, Electronic effects of ligand substitution on metal-organic framework photocatalysts: the case study of UiO-66, *Phys. Chem. Chem. Phys.* 17 (2015) 117–121, <https://doi.org/10.1039/c4cp04162c>.
- [21] C. Avci-Camur, J. Perez-Carvajal, I. Imaz, D. Maspoch, Metal acetylacetonates as a source of metals for aqueous synthesis of metal-organic frameworks, *ACS Sustain. Chem. Eng.* 6 (2018) 14554–14560, <https://doi.org/10.1021/acsschemeng.8b03180>.
- [22] Y. Li, Y. Liu, W. Gao, L. Zhang, W. Liu, J. Lu, Z. Wang, Y.J. Deng, Microwave-assisted synthesis of UiO-66 and its adsorption performance towards dyes, *CrystEngComm* 16 (2014) 7037–7042, <https://doi.org/10.1039/c4ce00526k>.
- [23] M. Taddei, P.V. Dau, S.M. Cohen, M. Ranocchiari, J.A. Van Bokhoven, F. Costantino, S. Sabatini, R. Vivani, Efficient microwave assisted synthesis of metal-organic framework UiO-66: optimization and scale up, *Dalton Trans.* 44 (2015) 14019–14026, <https://doi.org/10.1039/c5dt01838b>.
- [24] A. Huang, L. Wan, J. Caro, Microwave-assisted synthesis of well-shaped UiO-66-NH<sub>2</sub> with high CO<sub>2</sub> adsorption capacity, *Mater. Res. Bull.* 98 (2018) 308–313, <https://doi.org/10.1016/j.materresbull.2017.10.038>.
- [25] V.V. Butova, K.S. Veditsyna-Novikova, I.A. Pankin, K.M. Charykov, A.L. Trigub, A. V. Soldatov, Microwave synthesis and phase transition in UiO-66/MIL-140A system, *Microporous Mesoporous Mater.* 296 (2020), 109998, <https://doi.org/10.1016/j.micromeso.2020.109998>.
- [26] Z. Zhang, C.A. Tao, J. Zhao, F. Wang, J. Huang, J. Wang, Microwave-assisted solvothermal synthesis of UiO-66-NH<sub>2</sub> and its catalytic performance toward the hydrolysis of a nerve agent simulant, *Catalysts* 10 (2020) 1–11, <https://doi.org/10.3390/catal10091086>.
- [27] H. Reinsch, S. Waitschat, S.M. Chavan, K.P. Lillerud, N. Stock, A facile “green” route for scalable batch production and continuous synthesis of zirconium MOFs, *Eur. J. Inorg. Chem.* 2016 (2016) 4490–4498, <https://doi.org/10.1002/ejic.201600295>.
- [28] K. Chakarova, I. Strauss, M. Mihaylov, N. Drenchev, K. Hadjiivanov, Evolution of acid and basic sites in UiO-66 and UiO-66-NH<sub>2</sub> metal-organic frameworks: FTIR study by probe molecules, *Microporous Mesoporous Mater.* 281 (2019) 110–122, <https://doi.org/10.1016/j.micromeso.2019.03.006>.
- [29] Y.L. Wang, S. Zhanb, Y.F. Zhab, J. Bedia, J.J. Rodríguez, C. Belver, UiO-66 based metal organic frameworks for the photodegradation of acetaminophen under simulated solar irradiation, *J. Environ. Chem. Eng.* 9 (2021), 106087, <https://doi.org/10.1016/j.jece.2021.106087>.
- [30] P. Makula, M. Pacia, W. Macyk, How to correctly determine the band gap energy of modified semiconductor photocatalysts based on UV-vis spectra, *J. Phys. Chem. Lett.* 9 (2018) 6814–6817, <https://doi.org/10.1021/acs.jpclett.8b02892>.
- [31] M. Zeama, M. Morsy, S. Abdel-Azeim, M. Abdelnaby, A. Alloush, Z. Yamani, Photophysical and photocatalytic properties of structurally modified UiO-66, *Inorg. Chim. Acta* 501 (2020), 119287, <https://doi.org/10.1016/j.ica.2019.119287>.
- [32] K. Gelderman, L. Lee, S.W. Donne, Flat-band potential of a semiconductor: using the Mott-Schottky equation, *J. Chem. Educ.* 84 (2007) 25, <https://doi.org/10.1021/ed084p685>.
- [33] L.M. Peter, Photoelectrochemistry: from basic principles to photocatalysis, *RSC Energy Environ. Ser. R. Soc. Chem.* (2016) 1–28, <https://doi.org/10.1039/9781782622338-00001>.
- [34] T. Giannakopoulou, I. Papailias, N. Todorova, N. Boukos, Y. Liu, J. Yu, C. Trapalis, Tailoring the energy band gap and edges’ potentials of g-C<sub>3</sub>N<sub>4</sub>/TiO<sub>2</sub> composite photocatalysts for NO<sub>x</sub> removal, *Chem. Eng. J.* 310 (2017) 571–580, <https://doi.org/10.1016/j.cej.2015.12.102>.
- [35] Z. Rajah, M. Guiza, R.R.R. Solís, N. Becheikh, F.J.J. Rivas, A. Ouederni, Clopyralid degradation using solar-photocatalytic/ozone process with olive stone activated carbon, *J. Environ. Chem. Eng.* 7 (2019), 102900, <https://doi.org/10.1016/j.jece.2019.102900>.
- [36] M. Peñas-Garzón, W.H.M. Abdelraheem, C. Belver, J.J. Rodríguez, J. Bedia, D. Dionysiou, TiO<sub>2</sub>-carbon microspheres as photocatalysts for effective remediation of pharmaceuticals under simulated solar light, *Sep. Purif. Technol.* 275 (2021), 119169, <https://doi.org/10.1016/J.SEPUR.2021.119169>.
- [37] J.N. Miller, J.C. Miller, R.D. Miller, *Statistics and Chemometrics for Analytical Chemistry*, seventh ed., Pearson Education Limited, Harlow (United Kingdom), 2018.
- [38] D. Banerjee, W. Xu, Z. Nie, L.E.V. Johnson, C. Coghlan, M.L. Sushko, D. Kim, M. J. Schweiger, A.A. Kruger, C.J. Doonan, P.K. Thallapally, Zirconium-based metal-organic framework for removal of perchlorate from water, *Inorg. Chem.* 55 (2016) 8241–8243, <https://doi.org/10.1021/acs.inorgchem.6b01004>.
- [39] J. Ge, L. Liu, Y. Shen, Facile synthesis of amine-functionalized UiO-66 by microwave method and application for methylene blue adsorption, *J. Porous Mater.* 24 (2017) 647–655, <https://doi.org/10.1007/s10934-016-0301-1>.
- [40] T.K. Vo, V.N. Le, V.C. Nguyen, M. Song, D. Kim, K.S. Yoo, B.J. Park, J. Kim, Microwave-assisted continuous-flow synthesis of mixed-ligand UiO-66(Zr) frameworks and their application to toluene adsorption, *J. Ind. Eng. Chem.* 86 (2020) 178–185, <https://doi.org/10.1016/j.jiec.2020.03.001>.
- [41] J. Mehta, S. Dhaka, A.K. Paul, S. Dayananda, A. Deep, Organophosphate hydrolase conjugated UiO-66-NH<sub>2</sub> MOF based highly sensitive optical detection of methyl parathion, *Environ. Res.* 174 (2019) 46–53, <https://doi.org/10.1016/J.ENVRRES.2019.04.018>.
- [42] X. Chen, Y. Cai, R. Liang, Y. Tao, W. Wang, J. Zhao, X. Chen, H. Li, D. Zhang, NH<sub>2</sub>-UiO-66(Zr) with fast electron transfer routes for breaking down nitric oxide via photocatalysis, *Appl. Catal. B Environ.* 267 (2020), 118687, <https://doi.org/10.1016/j.apcatb.2020.118687>.
- [43] M. Fumanal, A. Ortega-Guerrero, K.M. Jablonka, B. Smit, I. Tavernelli, Charge separation and charge carrier mobility in photocatalytic metal-organic frameworks, *Adv. Funct. Mater.* 30 (2020), 2003792, <https://doi.org/10.1002/adfm.202003792>.
- [44] M.A. Nasalevich, M. Van Der Veen, F. Kapteijn, J. Gascon, Metal-organic frameworks as heterogeneous photocatalysts: advantages and challenges, *CrystEngComm* 16 (2014) 4919–4926, <https://doi.org/10.1039/c4ce00032c>.
- [45] Q. Chen, Q. He, M. Lv, Y. Xu, H. Yang, X. Liu, F. Wei, Selective adsorption of cationic dyes by UiO-66-NH<sub>2</sub>, *Appl. Surf. Sci.* 327 (2015) 77–85, <https://doi.org/10.1016/j.apsusc.2014.11.103>.
- [46] M. Rubio-Martínez, C. Avci-Camur, A.W. Thornton, I. Imaz, D. Maspoch, M.R. Hill, New synthetic routes towards MOF production at scale, *Chem. Soc. Rev.* 46 (2017) 3453–3480, <https://doi.org/10.1039/c7cs00109f>.
- [47] X. Fang, S. Wu, Y. Wu, W. Yang, Y. Li, J. He, P. Hong, M. Nie, C. Xie, Z. Wu, K. Zhang, L. Kong, J. Liu, High-efficiency adsorption of norfloxacin using octahedral UiO-66-NH<sub>2</sub> nanomaterials: dynamics, thermodynamics, and mechanisms, *Appl. Surf. Sci.* 518 (2020), 146226, <https://doi.org/10.1016/j.apsusc.2020.146226>.
- [48] N. Yin, K. Wang, Z. Li, Rapid microwave-promoted synthesis of Zr-MOFs: an efficient adsorbent for Pb(II) removal, *Chem. Lett.* 45 (2016) 625–627, <https://doi.org/10.1246/cl.160148>.
- [49] Z. Yang, X. Tong, J. Feng, S. He, M. Fu, X. Niu, T. Zhang, H. Liang, A. Ding, X. Feng, Flower-like BiOBr/UiO-66-NH<sub>2</sub> nanosphere with improved photocatalytic property for norfloxacin removal, *Chemosphere* 220 (2019) 98–106, <https://doi.org/10.1016/j.chemosphere.2018.12.086>.
- [50] V. Muelas-Ramos, M.J. Sampaio, C.G. Silva, J. Bedia, J.J. Rodríguez, J.L. Faria, C. Belver, Degradation of diclofenac in water under LED irradiation using combined g-C<sub>3</sub>N<sub>4</sub>/NH<sub>2</sub>-MIL-125 photocatalysts, *J. Hazard. Mater.* 416 (2021), 126199, <https://doi.org/10.1016/J.JHAZMAT.2021.126199>.
- [51] X. He, F. Deng, T. Shen, L. Yang, D. Chen, J. Luo, X. Luo, X. Min, F. Wang, Exceptional adsorption of arsenic by zirconium metal-organic frameworks: Engineering exploration and mechanism insight, *J. Colloid Interface Sci.* 539 (2019) 223–234, <https://doi.org/10.1016/j.jcis.2018.12.065>.
- [52] Z. Hasan, S.H. Jung, Removal of hazardous organics from water using metal-organic frameworks (MOFs): Plausible mechanisms for selective adsorptions, *J. Hazard. Mater.* 283 (2015) 329–339, <https://doi.org/10.1016/j.jhazmat.2014.09.046>.
- [53] C. Du, Z. Zhang, G. Yu, H. Wu, H. Chen, L. Zhou, Y. Zhang, Y. Su, S. Tan, L. Yang, J. Song, S. Wang, A review of metal organic framework (MOFs)-based materials for antibiotics removal via adsorption and photocatalysis, *Chemosphere* 272 (2021), 129501, <https://doi.org/10.1016/j.chemosphere.2020.129501>.
- [54] H. Diarmand-Khalilabad, A. Habibi-Yangjeh, D. Seifzadeh, S. Asadzadeh-Khaneghah, E. Vesali-Kermani, g-C<sub>3</sub>N<sub>4</sub> nanosheets decorated with carbon dots and CdS nanoparticles: novel nanocomposites with excellent nitrogen photofixation ability under simulated solar irradiation, *Ceram. Int.* 45 (2019) 2542–2555, <https://doi.org/10.1016/J.CERAMINT.2018.10.185>.



- [55] R. Yuan, Y. Zhu, B. Zhou, J. Hu, Photocatalytic oxidation of sulfamethoxazole in the presence of  $\text{TiO}_2$ : effect of matrix in aqueous solution on decomposition mechanisms, *Chem. Eng. J.* 359 (2019) 1527–1536, <https://doi.org/10.1016/J.CEJ.2018.11.019>.
- [56] M. Pelaez, A.A. de la Cruz, K. O'Shea, P. Falaras, D.D. Dionysiou, Effects of water parameters on the degradation of microcystin-LR under visible light-activated  $\text{TiO}_2$  photocatalyst, *Water Res.* 45 (2011) 3787–3796, <https://doi.org/10.1016/J.WATRES.2011.04.036>.
- [57] M.S. Alam, B.S.M. Rao, E. Janata, OH reactions with aliphatic alcohols: evaluation of kinetics by direct optical absorption measurement. A pulse radiolysis study, *Radiat. Phys. Chem.* 67 (2003) 723–728, [https://doi.org/10.1016/S0969-806X\(03\)00310-4](https://doi.org/10.1016/S0969-806X(03)00310-4).
- [58] E.M. Rodríguez, G. Márquez, M. Tena, P.M. Álvarez, F.J. Beltrán, Determination of main species involved in the first steps of  $\text{TiO}_2$  photocatalytic degradation of organics with the use of scavengers: The case of ofloxacin, *Appl. Catal. B Environ.* 178 (2015) 44–53, <https://doi.org/10.1016/j.apcatb.2014.11.002>.
- [59] C.L. Greenstock, R.W. Miller, The oxidation of tiron by superoxide anion. Kinetics of the reaction in aqueous solution and in chloroplasts, *BBA - Bioenergetics* 396 (1975) 11–16, [https://doi.org/10.1016/0005-2728\(75\)90184-X](https://doi.org/10.1016/0005-2728(75)90184-X).
- [60] W. Bors, M. Saran, C. Michel, Pulse-radiolytic investigations of catechols and catecholamines II. Reactions of Tiron with oxygen radical species, *BBA - Gen. Subj.* 582 (1979) 537–542, [https://doi.org/10.1016/0304-4165\(79\)90145-4](https://doi.org/10.1016/0304-4165(79)90145-4).
- [61] B.G. Ershov, E. Janata, M.S. Alam, A.V. Gordeev, A pulse radiolysis study of the reactions of the hydrated electron and hydroxyl radical with the oxalate ion in neutral aqueous solution, *High Energy Chem.* 42 (2008) 1–6, <https://doi.org/10.1134/s0018143908010013>.
- [62] C.K. Huang, T. Wu, C.W. Huang, C.Y. Lai, M.Y. Wu, Y.W. Lin, Enhanced photocatalytic performance of  $\text{BiVO}_4$  in aqueous  $\text{AgNO}_3$  solution under visible light irradiation, *Appl. Surf. Sci.* 399 (2017) 10–19, <https://doi.org/10.1016/j.apsusc.2016.12.038>.
- [63] W. He, J. Cai, X. Jiang, J.J. Yin, Q. Meng, Generation of reactive oxygen species and charge carriers in plasmonic photocatalytic  $\text{Au@TiO}_2$  nanostructures with enhanced activity, *Phys. Chem. Chem. Phys.* 20 (2018) 16117–16125, <https://doi.org/10.1039/C8CP01978A>.
- [64] Y. Wu, X. Li, Q. Yang, D. Wang, F. Yao, J. Cao, Z. Chen, X. Huang, Y. Yang, X. Li, Mxene-modulated dual-heterojunction generation on a metal-organic framework (MOF) via surface constitution reconstruction for enhanced photocatalytic activity, *Chem. Eng. J.* 390 (2020), 124519, <https://doi.org/10.1016/J.CEJ.2020.124519>.
- [65] Z. Wang, W. Ma, C. Chen, H. Ji, J. Zhao, Probing paramagnetic species in titania-based heterogeneous photocatalysis by electron spin resonance (ESR) spectroscopy—A mini review, *Chem. Eng. J.* 170 (2011) 353–362, <https://doi.org/10.1016/J.CEJ.2010.12.002>.
- [66] P.M. Wood, The potential diagram for oxygen at pH 7, *Biochem. J.* 253 (1988) 287–289, <https://doi.org/10.1042/BJ2530287>.
- [67] W.H. Koppenol, D.M. Stanbury, P.L. Bounds, Electrode potentials of partially reduced oxygen species, from dioxygen to water, *Free Radic. Biol. Med.* 49 (2010) 317–322, <https://doi.org/10.1016/J.FREERADBIOMED.2010.04.011>.
- [68] F. Ahmadijokani, R. Mohammadkhani, S. Ahmadiyouya, A. Shokrgozar, M. Reza kazemi, H. Molavi, T.M. Aminabhavi, M. Arjmand, Superior chemical stability of UiO-66 metal-organic frameworks (MOFs) for selective dye adsorption, *Chem. Eng. J.* 399 (2020), 125346, <https://doi.org/10.1016/j.cej.2020.125346>.
- [69] G. Wu, P. Li, D. Xu, B. Luo, Y. Hong, W. Shi, C. Liu, Hydrothermal synthesis and visible-light-driven photocatalytic degradation for tetracycline of Mn-doped  $\text{SrTiO}_3$  nanocubes, *Appl. Surf. Sci.* 333 (2015) 39–47, <https://doi.org/10.1016/j.apsusc.2015.02.008>.
- [70] K.Y.A. Lin, Y.T. Liu, S.Y. Chen, Adsorption of fluoride to UiO-66- $\text{NH}_2$  in water: stability, kinetic, isotherm and thermodynamic studies, *J. Colloid Interface Sci.* 461 (2016) 79–87, <https://doi.org/10.1016/j.jcis.2015.08.061>.
- [71] H. Molavi, A. Hakimian, A. Shojaei, M. Raeiszadeh, Selective dye adsorption by highly water stable metal-organic framework: Long term stability analysis in aqueous media, *Appl. Surf. Sci.* 445 (2018) 424–436, <https://doi.org/10.1016/j.apsusc.2018.03.189>.
- [72] J. Long, S. Wang, Z. Ding, S. Wang, Y. Zhou, L. Huang, X. Wang, Amine-functionalized zirconium metal-organic framework as efficient visible-light photocatalyst for aerobic organic transformations, *Chem. Commun.* 48 (2012) 11656–11658, <https://doi.org/10.1039/c2cc34620f>.
- [73] A. Dhakshinamoorthy, S. Navalon, A.M. Asiri, H. Garcia, Metal organic frameworks as solid catalysts for liquid-phase continuous flow reactions, *Chem. Commun.* 56 (2019) 26–45, <https://doi.org/10.1039/C9CC07953J>.
- [74] R.R. Solís, A. Gómez-Avilés, C. Belver, J.J. Rodríguez, J. Bedia, Microwave-assisted synthesis of  $\text{NH}_2$ -MIL-125(Ti) for the solar photocatalytic degradation of aqueous emerging pollutants in batch and continuous tests, *J. Environ. Chem. Eng.* 9 (2021), 106230, <https://doi.org/10.1016/J.JECE.2021.106230>.
- [75] I. Ahmed, S.H. Jung, Applications of metal-organic frameworks in adsorption/separation processes via hydrogen bonding interactions, *Chem. Eng. J.* 310 (2017) 197–215, <https://doi.org/10.1016/j.cej.2016.10.115>.
- [76] K.H. Wammer, M.T. Slattery, A.M. Stemig, J.L. Ditty, Tetracycline photolysis in natural waters: loss of antibacterial activity, *Chemosphere* 85 (2011) 1505–1510, <https://doi.org/10.1016/j.chemosphere.2011.08.051>.
- [77] S.R. Batchu, V.R. Panditi, K.E. O'Shea, P.R. Gardinali, Photodegradation of antibiotics under simulated solar radiation: implications for their environmental fate, *Sci. Total Environ.* 470–471 (2014) 299–310, <https://doi.org/10.1016/j.scitotenv.2013.09.057>.